CrystEngComm

Accepted Manuscript

ROYAL SOCIETY OF CHEMISTRY

www.rsc.org/crystengcomm

Graphical Abstract

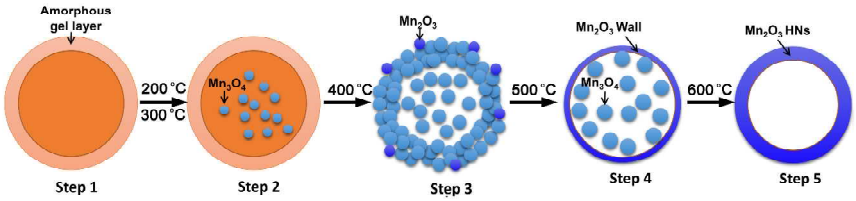

Well-defined Mn_2O_3 hollow nanofibers with a smooth wall were successfully fabricated by a single-spinneret electrospinning method. The possible formation mechanism was introduced based on the temperature-dependent experiments.

Cite this: DOI: 10.1039/c0xx00000x

www.rsc.org/xxxxxx

ARTICLE TYPE

Fabrication and formation mechanism of Mn_2O_3 hollow nanofibers by single-spinneret electrospinning

Guorui Yang,[a] Wei Yan, *[a,b] Jianan Wang[a] and Honghui Yang*[a]

Received (in XXX, XXX) Xth XXXXXXXXX 20XX, Accepted Xth XXXXXXXXX 20XX

DOI: 10.1039/b000000x

Mn_2O_3 hollow nanofibers (Mn_2O_3 HNs) have been prepared by direct annealing of electrospun polyvinylpyrrolidone (PVP)/manganese acetate composite nanofibers. The morphology, crystal structure and compositions of the Mn_2O_3 HNs were investigated by using the scanning electronmicroscopy (SEM), transmission electron microscopy (TEM), the X-ray diffraction (XRD), energy dispersive X-ray spectroscopy (EDS), X-ray photoelectron spectroscopy (XPS), respectively. The results indicated that composite nanofibers after calcined at high temperature still remain fibrous morphology with a fascinating hollow structure. The resultant HNs are Mn_2O_3 with high purity. The temperature-dependent experiments were carried out to monitor the evolution process of Mn_2O_3 HNs. The well-defined Mn_2O_3 HNs is the end product of the reversed crystallization during the annealing process.

1. Introduction

In past decades, great efforts have been devoted to the fabrication and characterization of nanosized materials as well as devices assembled from them. Functional one dimensional (1D) nanostructures such as nanorods, nanowirs, nanofibers, nanotubes and so on,[1-5] are of particular interest with respect to their potential in a wealth of applications that include gas sensor, [6, 7] optoelectronic materials,[8] catalyst,[9-11] energy store,[12-14] etc. Among different shapes of 1D nanostructures, nanotubes with modulated compositions have the advantages of large specific surface areas,[15] anisotropic properties and the unique hollow structure feature,[16] which are the desirable properties for applications such as Li-ion batteries,[17] dye-sensitized solar cells,[18] photocatalytic catalysts[19] and sensors.[20] Since the first discovery of the carbon nanotubes,[21] many procedures including self-assembly,[22] templates directed process,[23, 24] hydrothermal,[25] chemical vapor deposition [26] and co-electrospinning[27] have been reported for the preparation of 1D nanotubes. However, these methods often suffer from tedious procedures, templates and catalysts. The template process has been widely used to produce hollow nanostructures. Nevertheless, the resultant materials were limited by the morphology and structure of the templates. Moreover, the introduction of template may case heterogeneous impurities and increases manufacture cost.[28] self-assembly method was proven to be an effective route to fabrication of nano- to micro tubules, notwithstanding the length of the obtained tubules is usually in the micro- or submicroscale, and the formation of tubular structures is always incidental.[29] It is urgently important to develop a straightforward method with features of facility, versatility and economic cost to synthesize 1D nanotubes.

As an important member in Manganese oxide family (MnO, Mn_3O_4, Mn_2O_3, Mn_5O_8 and MnO_2), Mn_2O_3 exhibits distinctive chemical and physical properties. It has been widely explored as an environment-friendly catalyst to remove carbon monoxide and nitrogen oxide from waste gas,[30, 31] the inexpensive precursor for producing soft magnetic materials, the promising absorbent for water treatment[32, 33] and the efficient electrode material of rechargeable lithium batteries.[34, 35] Therefore, great efforts have been paid to the synthesis of Mn_2O_3 with different morphologies ranging from one- to three-dimensional structures including rods, wires, cubes, octahedral, hollow structures, etc.[35-40] It has been reported that the properties of nanomaterials depend on not only their chemical components, but also their structures, morphologies, dimensions and size distributions.[41] Hence, controlled preparation of Mn_2O_3 with desired morphology, shape, and size may induce fascinating properties and wider applications. Previous researchers have claimed that the capacity retention of Mn_2O_3 material is generally very poor, when it was used as an anode material for lithium ion batteries.[34, 42] In contrast, straw-sheaf-shaped Mn_2O_3 had an outstanding performance in the capacity retention.[43] Despite these successes, the morphology controlled synthesis of Mn_2O_3 hollow nanofibers is still a great challenge and highly desirable.

Electrospinning was regarded as a cost effective and flexible platform for 1D nanostructures preparing, and several typical 1D nanostructures (solid, hollow, belt and porous) have been facilely prepared in previous work.[44, 45] By controlling the precursory components and processing parameters, the morphology, size, structure and composition of the eletrospun products can be conveniently tuned in a wide range.[16] In recent years, a variety of HNs were successfully obtained by electrospinning that can be classified into three major methods which are inclusive of TUFT (Tubes by Fibers Templates) process,[46] coaxial electrospinning route[47] and single-nozzle co-electrospinning technique.[28, 48]

However, these three methods are less than satisfactory. For instance, different coating processes involved in TUFT process such as chemical vapor deposition and atomic layer deposition, make high demand on apparatus and result in a multistep process.[49] Coaxial electrospinning is affected by many factors, such as miscibility or immiscibility of the pair of solutions, viscosity ratio, interfacial tension and so forth. As a result, it is difficult to achieve good concentricity of the core and shell materials in the electrospun fibers.[50] For single-nozzle co-electrospinning one must choose two different appropriate polymers to form phase separation.[3] Using one-pot single-spinneret electrospinng to prepare HNs will be an ideal solution which can avoid the disadvantages as mentioned above. To date, numerous hollow fibers with different compositions such as Fe_2O_3,[51] SnO_2,[10, 52] TiO_2,[15, 53] NiO,[54] $CoFe_2O_4$,[55] ZnO-SnO_2[56] etc. have been fabricated by the one-pot single-spinneret electrospinng method. To the best of our knowledge, no one has reported the detailed study on the synthesis of Mn_2O_3 HNs as well as the possible formation mechanism.

Motivated by the above concerns, for the first time we proposed a one-pot single-spinneret electrospinning technique to prepare Mn_2O_3 HNs. Compared with other methods, neither a coating procedure nor a special spinner is required, HNs could be fabricated by simply annealing composite fibers. The temperature-dependent experiments were carried out to monitor the evolution process of the Mn_2O_3 HNs. Also, based on the experimental observations, a possible formation mechanism of the Mn_2O_3 HNs was also proposed.

2. Experiment

2.1. Preparation of Mn_2O_3 hollow nanofibers

Poly (vinyl pyrrolidone) (PVP, Mw = 13 000 00), manganese acetate ($Mn(CH_3COO)_2{\cdot}4H_2O$) and mixture of methyl alcohol and acetic acid (weight ratio 4:1) were mixed together followed by vigorous stirring for 6 h. 10 mL of the precursor solution was loaded into a syringe with a stainless steel needle which was connected to a high-voltage supply. A voltage of 12 kV was used to the spinneret. A sheet of aluminum foil was used as the collector and it was placed 12 cm away from the needle. The as-spun fibers were calcined at 600 ºC for 4 h.

2.2. Characterization.

The morphologies of the products were examined using SEM (JEOL JSM 6700F field emission instrument) and EDS was performed on JEOL JSM 6460. TEM, high revolution TEM (HRTEM) and selected area electron diffraction (SAED) images were obtained by a JEOL JEM2100 instrument. XRD (X'pert MPD Pro (PANalytical Co.) diffractmeter using Cu-Kα radiation (40 kV, 40 mA)) analyses were carried out. The elemental information was studied using the XPS measurement (Axis Ultra, Kratos (UK) at monochromatic Al Kα radiation (150 W, 15 kV and 1486.6 eV). The thermogravimetric analysis (TG) was carried out on a Perki Elemer TGA-7 at a heating rate of 5 ^oC min^{-1} in air.

3. Results and discussion

3.1. Structures and morphologies of Mn_2O_3 HNs

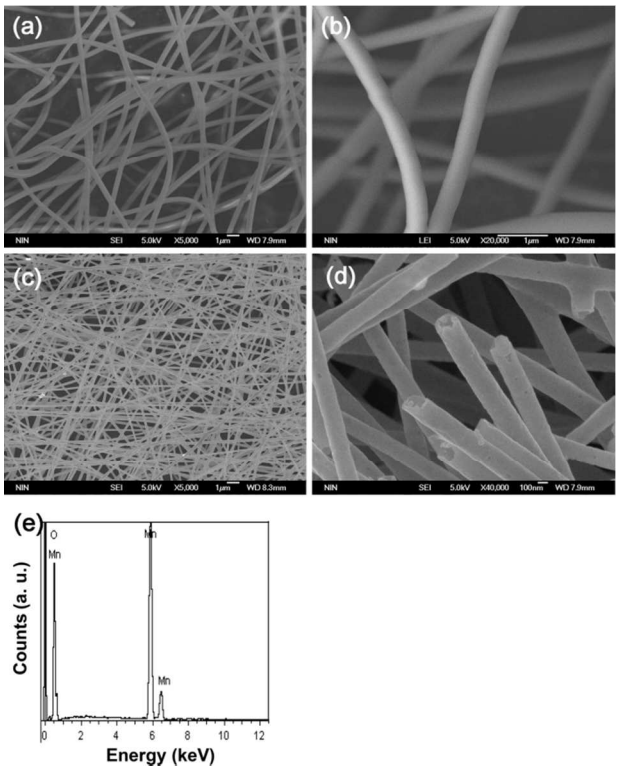

Fig.1 (a, b) SEM images of uncalcined Mn_2O_3 HNs with different magnifications, (c, d) Mn_2O_3 HNs with different magnifications, (e) EDS spectrum of sample Mn_2O_3 HNs.

Fig. 1a-d show the morphologies of the as-prepared samples at different magnifications. Fig. 1a and b indicate that the uncalcined fibers possess a smooth surface due to the amorphous nature and align in a random orientation resulting from the bending instability of the spinning jet.[57] The fibers are quite uniform with a diameter of about *ca.* 430 nm. After calcination at 600 ^oC, a well-defined 1D structure was still retained, which indicated that heat treatment do not destroy the fibrous morphology. However, the diameter of fibers drastically shrinks to about 200 nm due to the decomposition of PVP and crystallization of Mn_2O_3.[58] Fig. 1d depicts the morphology of the Mn_2O_3 HNs at a higher magnification, clearly indicating a large quantity of tube-like structures. The chemical compositions of the sample was further characterized by EDS. Fig. 1e is the EDS spectrum of the Mn_2O_3 HNs, and it indicates that the obtained HNs were mainly composed of Mn and O.

TEM observations were carried out to substantiate more detailed information about the morphology and the crystal structure of the Mn_2O_3 HNs. It can be found from Fig. 2a that Mn_2O_3 HNs have a relatively smooth surface, which is consistent with the SEM results. The strong contrast between the dark edges and the light center further demonstrates that the Mn_2O_3 HNs are all hollow (inset of Fig. 2a), and reveals the well-defined tubular nanostructures with diameters of 200 nm and wall thicknesses of 30 nm. The lattice fringes with spacing of 0.38 nm can be clearly observed in Fig. 2b, which is in agreement with spacing of (211) planes of Mn_2O_3. The 2D electron diffraction pattern (inset of Fig. 2b) indicates that the as-prepared HNs had a single crystalline structure, which may be the reason for the formation of Mn_2O_3 HNs smooth surface. However, we were not able to

identify a

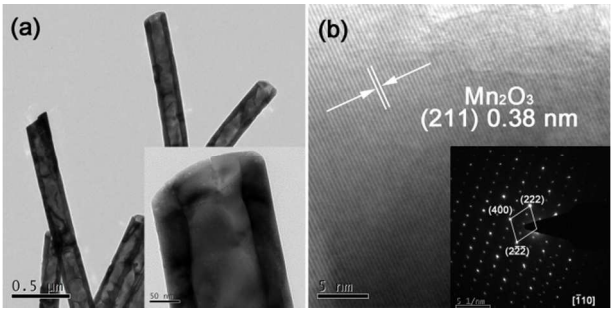

Fig. 2 (a) TEM image of the Mn_2O_3 HNs, inset is lager magnification TEM image. (b) HRTEM image of the Mn_2O_3 HNs, inset is the SAED collected from a single hollow nanofiber.

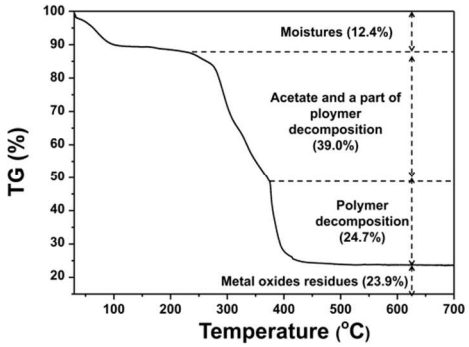

Fig. 3 TG analysis of the Mn_2O_3 precursor nanofibers

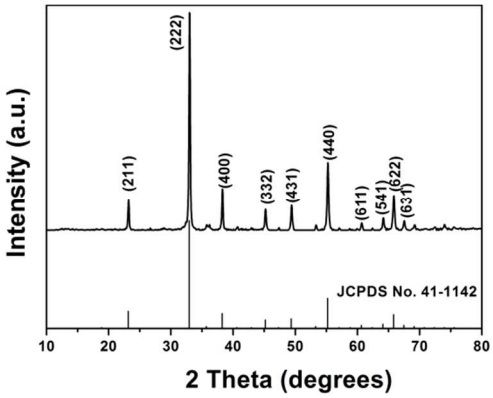

Fig. 4 XRD patterns of the Mn_2O_3 HNs

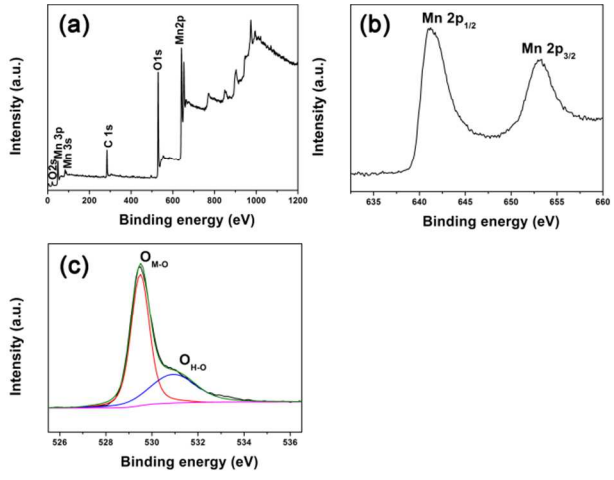

Fig.5 (a) XPS fully scanned spectra of pristine Mn_2O_3 HNs; High resolution XPS spectrum for (b) Mn 2p and (c) O 1s.

reasonable explanation for the evolution of the single crystalline structure.

In order to display the decomposition process of the precursor fibers, TG analysis was carried out. As illustrated in Fig. 3, the TG curve elucidates three obvious weight loss processes. The first mass loss is about 12.4 % before 215 °C, which is resulted from evaporation of acetic acid, methyl alcohol and a little water. The second obvious weight loss (*ca.*39.0 %) between 215 and 375 °C is mainly ascribed to the decomposition of manganese acetate and a fraction of PVP.[13] The further weight loss (24.7 %) in the range of 375 and 500 °C is due to the degradation of almost of residual PVP. [59] When the temperature is higher than 500 °C, no discernible weight loss was observed indicating that the precursor is converted to Mn_2O_3 HNs completely.

Crystal structures and phase compositions of the Mn_2O_3 HNs were confirmed by XRD measurements. As observed in Fig. 4, all diffraction peaks are well indexed to pure Mn_2O_3 with spinel structure (JCPDS No. 41-1442), where the diffraction peaks at 2θ values of 23.1°, 33.0°, 38.3°, 45.2°, 49.3°, 55.2°, 60.6°, 64.2°, 65.8° and 67.5° are ascribed to the reflections of (211), (222), (400), (332), (431), (440), (611), (541), (622) and (631) planes of the spinel Mn_2O_3, respectively. Notably, only characteristic peaks of Mn_2O_3 existed in the sample, and no peak from the impurities such as MnO and Mn_3O_4 could be detected, indicating that the HNs are Mn_2O_3 with high purity.

The chemical compositions and electronic structures of the Mn_2O_3 HNs were analyzed by XPS. Fig. 5a exhibits the survey spectrum, from which it can be clearly observed that the peaks of Mn and O coexist in Mn_2O_3 nanofibers. This result is well witnessed by the outcomes of EDS and XRD. The high-resolution XPS spectra of Mn 2p and O1s are showed in Fig. 5b and c, respectively. The Mn 2p orbital region (Fig. 5b) shows the binding energies of Mn $2p_{1/2}$ and Mn $2p_{3/2}$ peaks at 641.21 eV and 653.21eV, respectively. The splitting energy of 12.0 eV between Mn $2p_{3/2}$ and Mn $2p_{1/2}$ is a typical value for Mn^{3+}.[60] As shown in Fig. 5c, the shape of asymmetric peaks of O 1s spectrum indicate that crystal lattice oxygen (O_{M-O}, 529.51 eV) and surface hydroxyl groups (O_{H-O}, 530.91 eV) presented simultaneously in the Mn_2O_3 HNs [44]. From this brief analysis, it is realistic to propose that pure Mn_2O_3 HNs were successfully synthesized in this work.

3.2. Formation mechanism of the Mn_2O_3 HNs

TEM observations (Fig. 6) and XRD measurements (Fig. 7) were purposely carried out to unveil that how Mn_2O_3 HNs evolve during heat treatment. Representative TEM images of the as-made fibers calcined at 200 °C are displayed in Fig. 6a and b. The morphology of the sample is nearly the same with the precursor fibers except that there exists many tiny particles in the core region of the fibers (Fig. 6b). As noted, a gel layer is formed on the shell layer. The white lines in Fig. 6 indicate the boundaries between the shell layer and the core region. Diffraction peaks appearing at 2θ of 18.0°, 28.9°, 32.4°, 36.2°, 58.6° and 59.9° in the XRD pattern (Fig. 7a) are well attributed to those of Mn_3O_4 (JCPDS No. 24-0734), corresponding to its (101), (112), (103),

(211), (321) and (224) facets, respectively. Fig. 6c and d illustrate TEM images of samples when the heating temperature rises to

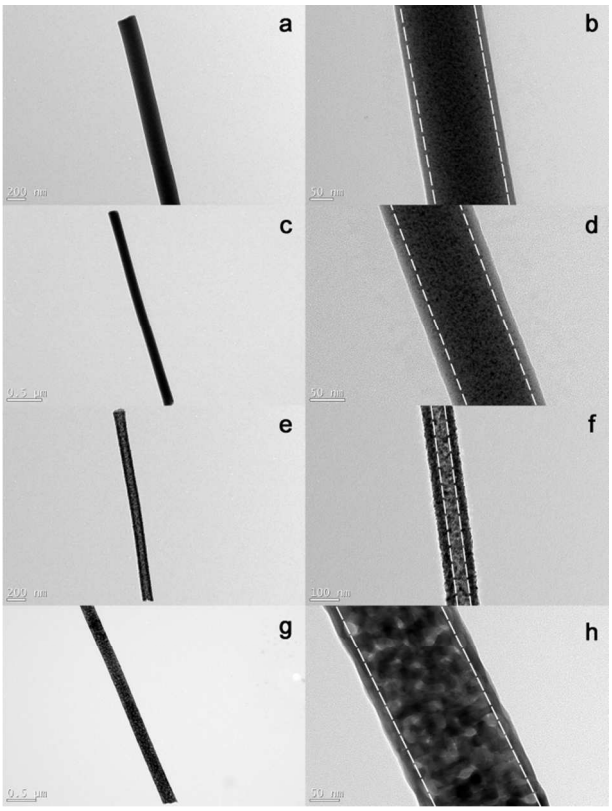

Fig. 6 TEM images of Mn_2O_3 precursor nanofibers heat treated at various temperatures: 200 °C (a 0and b), 300 °C (c and d), and 400 °C (e and f), 500 °C (g and h).

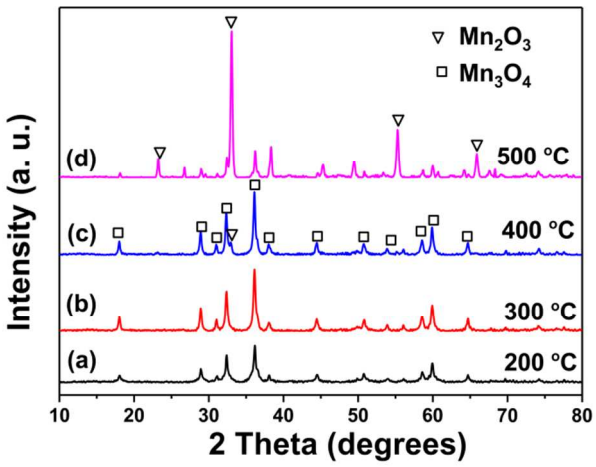

Fig. 7 XRD patterns of Mn_2O_3 precursor nanofibers annealed at different temperatures.

300 °C. The morphology of the fibers remains unchanged, while the crystallinity of the Mn_3O_4 particles pronounced as evidenced by the increase of diffraction peaks intensity. Upon raising the heating temperature to 400 °C, the gel layer disappeared; alternatively, a new porous layer constructed by nanoparticles is introduced (Fig. 6e and f). It reflects that at this evolution stage, the PVP molecules are subject to a thermal decomposition. The XRD pattern (Fig. 7c) and shows the presence of a new sharp diffraction peak at a 2θ of 33.0°, corresponding to the (222) facet of Mn_2O_3 (JCPDS No. 41-1442). Moreover, HRTEM images (Fig. S1a) confirm coexistence of Mn_3O_4 and Mn_2O_3 in the sample

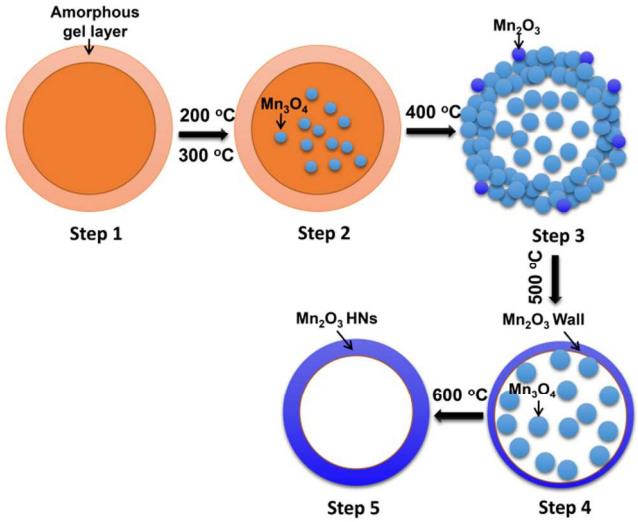

Scheme 1 Possible formation mechanism of Mn_2O_3 HNs.

calcined at 400 °C. As the temperature increasing, the XRD pattern (Fig. 7d) indicates that two distinct components, Mn_3O_4 and Mn_2O_3, are cleverly integrated after annealed process at 500 °C. The shell layer becomes a well-defined nanotube wall because of the transition from Mn_3O_4 to Mn_2O_3, as suggested by the decreased intensity of the peaks of Mn_3O_4 from the XRD pattern and the HRTEM images (Fig. S1 b and c). In addition, the fiber core region are resembles a chain of connected nanoparticles (Fig. 6 g and h). Simultaneously, the nanoparticles in fibers become larger due to the higher crystallization temperature. When heated to 600 °C, all diffraction peaks belonging to Mn_3O_4 are completely missing, which is ascribed to the ultimate conversion of Mn_3O_4 to Mn_2O_3.

Based on the experimental observations, a possible formation mechanism of the Mn_2O_3 HNs is proposed as following and the overall evolution process of the HNs is displayed in Scheme 1. Firstly, during the electrospinning process, PVP molecular chains were positively charged because the precursor solution was applied with a high-voltage generator. The positively charged PVP molecular chains would migrate to the surface of the jets;[61] consequently, a gel shell was formed on the surface of the precursor fibers associated with solvent evaporation and rapid phase separation (scheme 1 step 1). This gel layer plays an important role in maintaining the fibrous structure during the calcination process. The distance between needle and collector and the solvent factor play important roles during the gel layer formation, further influence the final product morphology. There should be an optimum distance which favours the evaporation of solvent to form gel layer (Fig. S2). Likewise, the solvent should possess a suitable volatile property that guarantees the generation of the gel layer (Fig. S3). During heat treatment, the gel layer became rigid, which gave rise to a temperature gradient that the core region possessed a higher temperature than the shell layer.[11] When the temperature rose above the decomposed point of the manganese acetate, Mn_3O_4 was produced. As a result, Mn_3O_4 tiny

particles preferentially formed in the core region of the fibers (Scheme 1 step 2) due to the relatively higher temperature in fiber core region. As the annealing temperature increasing, the PVP in the gel layer are eliminated by heat treatment (Scheme 1 step 3). Meanwhile, the Mn_3O_4 located near the surface of the precursor fibers was exposed to air, resulting in the formation of Mn_2O_3 tiny particles, whereas most of the Mn_3O_4 inside the fibers was unable to change because of lack of oxygen. As the temperature reached 500 ºC, the Mn_3O_4 would serve as crystal precursor for Mn_2O_3 growth and crystallization, which resulted in the formation of heterostructured core/shell fibers with Mn_2O_3 as shell and Mn_3O_4 as core (Scheme 1 step 5). When the sample was further heated up to 600 ºC, Mn_3O_4 could be entirely oxidized to Mn_2O_3 from the Mn_2O_3/Mn_3O_4 interface to core region of the nanofibers. The Mn_3O_4 continuously migrates to the Mn_2O_3/ Mn_3O_4 interface as precursor reactant for Mn_2O_3, and leave a hollow structure in the core region. Recently, Zhou and co-workers discovered a novel mechanism for a crystal growth process, reversed crystallization.[63, 64] Such crystallization mechanism has been generally employed to explain the formation processes of hollow and core/shell structures in several inorganic systems such as zeolites, perovskites, metal oxides, mesoporous silicates and metal.[65-67] This reversed crystal growth can be briefly divided into three stages: (I) aggregation of precursor nanoparticles, (II) surface crystallization, (III) surface-to-core extension of recrystallization. Our work may also obey the reversed crystallization, step 1 and step 2 in scheme 1 are analogous to the aforementioned stage (I), in which the Mn_3O_4 as precursor nanoparticles for Mn_2O_3 are generated and aggregated. Step 3-4 represent the stage (II), Mn_2O_3 shell layer start to crystallization on the surface by consuming precursor Mn_3O_4 nanoparticles (Fig. S1 b and c). Obviously, step 4-5 is corresponding to stage (III), surface-to-core extension of recrystallization result in the formation of single-crystal Mn_2O_3 HNs. The present work should provide a meaningful evidence for the reversed crystallization in gaseous phase circumstance rather than the most studied liquid phase environment.

4. Conclusions

In summary, we have described that Mn_2O_3 HNs could be directly synthesized via a simple single-needle electrospinning process. Both SEM observations and TEM images confirm that the Mn_2O_3 HNs possess a continuous morphology and a well-defined hollow structure. The diameter of the as-prepared Mn_2O_3 HNs is around 200 nm and the wall thickness is of *ca.* 30 nm. The temperature-dependent experiments were carried out to minor the evolution process of Mn_2O_3 HNs. The Mn_3O_4 precursor preferentially crystalized in the core region of the fibers. Subsequently, the PVP was eliminated by the high temperature treatment, meanwhile, the Mn_3O_4 changed to Mn_2O_3 at the surface. The core-region Mn_3O_4 migrated to the surface continuously due to the reaction from Mn_3O_4 to Mn_2O_3. Finally, Mn_2O_3 hollow nanofiers were obtained. This work suggests that electrospinning technique offers an additional means to fine tune the phase structure and morphology of 1D nanostructures, enabling the fabrication of complex architectures. Metal oxides are widely used in many technologically important fields such as catalysis, sensors, and Li-ion batteries. To achieve optimal performances, HNs with controlled crystalline structures and spatial distribution of each component are often desired. All these features make the electrospinning technique an ideal platform for studying the structure-property relationship, which will be beneficial to the design of high-performance materials such as catalysts, sensors and electrodes for batteries.

Acknowledgment

This work is supported by the Fundamental Research Funds for the Central Universities of China (2011JDGZ15); National Natural Science Foundation for the Youth (No.51308452, No.21307098).

Notes and references

[a] *Department of Environmental Science & Engineering, Xi'an Jiaotong University, Xi'an 710049, China. Fax:86 029 82664731; Tel:86 13032912105; E-mail: yanwei@mail.xjtu.edu.cn.*
[b] *State Key Laboratory of Multiphase Flow in Power Engineering, Xi'an Jiaotong University, Xi'an 710049, China.*

†Electronic Supplementary Information (ESI) available: HRTEM images of Mn_2O_3 percursor nanofibers calcined at 400 ºC and 500ºC, SEM micrographs of Mn_2O_3 with different capillary-collector distances. See DOI: 10.1039/b000000x/

1. H. Y. Chen, T. L. Zhang, J. Fan, D. B. Kuang and C. Y. Su, ACS Appl. Mater. Interfaces, 2013, **5**, 9205-9211.
2. G. Wang, H. Wang, Y. Ling, Y. Tang, X. Yang, R. C. Fitzmorris, C. Wang, J. Z. Zhang and Y. Li, *Nano Lett.*, 2011, **11**, 3026-3033.
3. G. Zhang, H. Duan, B. Lu and Z. Xu, *Nanoscale*, 2013, **5**, 5801-5808.
4. Z.-X. Yang, P. Zhang, W. Zhong, Y. Deng, C.-T. Au and Y.-W. Du, *CrystEngComm*, 2012, **14**, 4298-4305.
5. X. Meng, D.-W. Shin, S. M. Yu, J. H. Jung, H. I. Kim, H. M. Lee, Y.-H. Han, V. Bhoraskar and J.-B. Yoo, *CrystEngComm*, 2011, **13**, 3021-3029.
6. C. Zhao, G. Zhang, W. Han, J. Fu, Y. He, Z. Zhang and E. Xie, *CrystEngComm*, 2013, **15**, 6491-6497.
7. T. Maiyalagan, J. Sundaramurthy, P. S. Kumar, P. Kannan, M. Opallo and S. Ramakrishna, *Analyst*, 2013, **138**, 1779-1786.
8. C. Peng, G. Li, D. Geng, M. Shang, Z. Hou and J. Lin, *Mater. Res. Bull.*, 2012, **47**, 3592-3599.
9. S. S. Lee, H. Bai, Z. Liu and D. D. Sun, *Appl. Catal. B*, 2013, **140-141**, 68-81.
10. X. Wang, H. Fan and P. Ren, *Catal. Commun.*, 2013, **31**, 37-41.
11. G. Yang, W. Yan, Q. Zhang, S. Shen and S. Ding, *Nanoscale*, 2013, **5**, 12432-12439.
12. Y. L. Cheah, V. Aravindan and S. Madhavi, *ACS Appl. Mater. Interfaces*, 2013, **5**, 3475-3480.
13. L. Lang and Z. Xu, *ACS Appl. Mater. Interfaces*, 2013, **5**, 1698-1703.
14. S.-H. Choi, D. Hwang, D.-Y. Kim, Y. Kervella, P. Maldivi, S.-Y. Jang, R. Demadrille and I.-D. Kim, *Adv. Funct. Mater.*, 2013, **23**, 3146-3155.
15. Y. Cheng, W. Huang, Y. Zhang, L. Zhu, Y. Liu, X. Fan and X. Cao, *CrystEngComm*, 2010, **12**, 2256-2260.
16. G. Dong, X. Xiao, M. Peng, Z. Ma, S. Ye, D. Chen, H. Qin, G. Deng, Q. Liang and J. Qiu, *RSC Adv.*, 2012, **2**, 2773-2782.
17. J. Wang, Y. Yu, L. Gu, C. Wang, K. Tang and J. Maier, *Nanoscale*, 2013, **5**, 2647-2650.
18. X. Wang, G. He, H. Fong and Z. Zhu, *J. Phys. Chem. C*, 2013, **117**, 1641-1646.
19. C. Zhu, Y. Li, Q. Su, B. Lu, J. Pan, J. Zhang, E. Xie and W. Lan, *J. Alloys Compd.*, 2013, **575**, 333-338.
20. C. Zhao, G. Zhang, W. Han, J. Fu, Y. He, Z. Zhang and E. Xie, *CrystEngComm*, 2013, **15**, 6491.
21. S. Iijima, *Nature*, 1991, **354**, 56-58.

22. M. Remskar, A. Mrzel, Z. Skraba, A. Jesih, M. Ceh, J. Demšar, P. Stadelmann, F. Lévy and D. Mihailovic, *Science*, 2001, **292**, 479-481.
23. W. Chen, R. Rakhi and H. Alshareef, *J. . Mater. Chem. A*, 2013, **1**, 3315-3324.
24. S. Cho, D.-H. Kim, B.-S. Lee, J. Jung, W.-R. Yu, S.-H. Hong and S. Lee, *Sens. Actuators B* 2012, **162**, 300-306.
25. H.-H. Ou and S.-L. Lo, *Sep. Purif. Technol.*, 2007, **58**, 179-191.
26. Z.-h. Hu, S.-m. Dong, J.-b. Hu, Z. Wang, B. Lu, J.-s. Yang, Q.-g. Li, B. Wu, L. Gao and X.-y. Zhang, *Carbon*, 2013, **52**, 624.
27. D. Li and Y. Xia, *Nano Lett.*, 2004, **4**, 933-938.
28. W. Wang, J. Zhou, S. Zhang, J. Song, H. Duan, M. Zhou, C. Gong, Z. Bao, B. Lu, X. Li, W. Lan and E. Xie, *J. Mater. Chem.*, 2010, **20**, 9068-9072.
29. S. Zhan, D. Chen, X. Jiao and C. Tao, *J. Phys. Chem. B*, 2006, **110**, 11199-11204.
30. C. Zhang, L. Han, W. Liu, H. Yang, X. Zhang, X. Liu and Y. Yang, *CrystEngComm*, 2013, **15**, 5150-5155.
31. J. Xu, Y.-Q. Deng, Y. Luo, W. Mao, X.-J. Yang and Y.-F. Han, *J. Catal.*, 2013, **300**, 225-234.
32. J. Cao, Y. Zhu, L. Shi, L. Zhu, K. Bao, S. Liu and Y. Qian, *Eur. J. Inorg. Chem.*, 2010, **2010**, 1172-1176.
33. E. Saputra, S. Muhammad, H. Sun, H.-M. Ang, M. O. Tadé and S. Wang, *Appl. Catal. B*, 2013, **142-143**, 729-735.
34. Y. Deng, Z. Li, Z. Shi, H. Xu, F. Peng and G. Chen, *RSC Adv.*, 2012, **2**, 4645-4647.
35. L. Hu, Y. Sun, F. Zhang and Q. Chen, *J. Alloys Compd.*, 2013, **576**, 86-92.
36. Q. Javed, F. P. Wang, M. Y. Rafique, A. M. Toufiq, Q. S. Li, H. Mahmood and W. Khan, *Nanotechnology*, 2012, **23**, 415603.
37. J. Cao, Q. Mao and Y. Qian, *J. Solid State Chem.*, 2012, **191**, 10-14.
38. Y. G. Zhang, J. Chen, B. J. Huang and D. P. Li, *Adv. Mater. Res.*, 2011, **233**, 2252-2257.
39. J. Cao, Y. Zhu, K. Bao, L. Shi, S. Liu and Y. Qian, *J. of Phys. Chem. C*, 2009, **113**, 17755-17760.
40. W.-N. Li, L. Zhang, S. Sithambaram, J. Yuan, X.-F. Shen, M. Aindow and S. L. Suib, *J. of Phys. Chem. C*, 2007, **111**, 14694-14697.
41. J. Wang, G. Zhu, L. Deng, L. Kang, Z. Hao and Z. Liu, *CrystEngComm*, 2012, **14**, 8253-8260.
42. X. Fang, X. Lu, X. Guo, Y. Mao, Y.-S. Hu, J. Wang, Z. Wang, F. Wu, H. Liu and L. Chen, *Electrochem. Commun.*, 2010, **12**, 1520-1523.
43. Y. Qiu, G.-L. Xu, K. Yan, H. Sun, J. Xiao, S. Yang, S.-G. Sun, L. Jin and H. Deng, *J. Mater. Chem.*, 2011, **21**, 6346-6353.
44. G. Yang, Q. Zhang, W. Chang and W. Yan, *J. Alloys Compd.*, 2013, **580**, 29-36.
45. S. Cavaliere, S. Subianto, I. Savych, D. J. Jones and J. Rozière, *Energy Environ.Sci.*, 2011, **4**, 4761-4785.
46. S. H. Choi, G. Ankonina, D. Y. Youn, S. G. Oh, J. M. Hong, A. Rothschild and I. D. Kim, *ACS Nano*, 2009, **3**, 2623-2631.
47. X. Zhang, V. Aravindan, P. S. Kumar, H. Liu, J. Sundaramurthy, S. Ramakrishna and S. Madhavi, *Nanoscale*, 2013, **5**, 5973-5980.
48. K. Tang, Y. Yu, X. Mu, P. A. van Aken and J. Maier, *Electrochem. Commun.*, 2013, **28**, 54-57.
49. J. Zhao, Y. Cheng, X. Yan, D. Sun, F. Zhu and Q. Xue, *CrystEngComm*, 2012, **14**, 5879-5885.
50. B. Liu and L. Peng, *J. Alloys Compd.*, 2013, **571**, 145-152.
51. S. Chaudhari and M. Srinivasan, *J. Mater. Chem.*, 2012, **22**, 23049-23056.
52. C. Gao, X. Li, B. Lu, L. Chen, Y. Wang, F. Teng, J. Wang, Z. Zhang, X. Pan and E. Xie, *Nanoscale*, 2012, **4**, 3475-3481.
53. L. Lang, D. Wu and Z. Xu, *Chem. Eur. J*, 2012, **18**, 10661-10668.
54. B. Ren, M. Fan, Q. Liu, J. Wang, D. Song and X. Bai, *Electrochim. Acta*, 2013, **92**, 197-204.
55. J. Fu, J. Zhang, Y. Peng, J. Zhao, G. Tan, N. J. Mellors, E. Xie and W. Han, *Nanoscale*, 2012, **4**, 3932-3936.
56. L. Xu, R. Xing, J. Song, W. Xu and H. Song, *J Mater. Chem. C*, 2013, **1**, 2174-2182.
57. G. Yang, W. Chang and W. Yan, *J. Sol-Gel Sci. Technol.*, 2013, **69**, 473-479.
58. G. Yang, W. Yan, J. Wang and H. Yang, *Mater. Lett.*, 2014, **122**, 117-120.
59. Y. Zhang, J. Li, Q. Li, L. Zhu, X. Liu, X. Zhong, J. Meng and X. Cao, *J. Colloid Interface Sci.*, 2007, **307**, 567-571.
60. J. G. Kim, S. H. Lee, Y. Kim and W. B. Kim, *ACS Appl. Mater. Interfaces*, 2013, **5**, 11321-11328.
61. J. H. He and Y. Q. Wan, *Polymer*, 2004, **45**, 6731-6734.
62. J. Jiang, J. Luo, J. Zhu, X. Huang, J. Liu and T. Yu, *Nanoscale*, 2013, **5**, 8105-8113.
63. X. Chen, M. Qiao, S. Xie, K. Fan, W. Zhou and H. He, *J. Am. Chem. Soc.*, 2007, **129**, 13305-13312.
64. H. Greer, P. S. Wheatley, S. E. Ashbrook, R. E. Morris and W. Zhou, *J. Am. Chem. Soc.*, 2009, **131**, 17986-17992.
65. X. Yang, J. Fu, C. Jin, J. Chen, C. Liang, M. Wu and W. Zhou, *J. Am. Chem. Soc.*, 2010, **132**, 14279-14287.
66. H. F. Greer, *Mater. Sci. Technol.*, 2014, **30**, 611-626.
67. M. L. Moreira, J. Andrés, V. R. Mastelaro, J. A. Varela and E. Longo, *CrystEngComm*, 2011, **13**, 5818-5824.